Self-cleaning compact heat exchangers: the role of two-phase flow patterns in design and optimization

Dario Maggiolo[a,b], Srdjan Sasic[a], Henrik Ström[a]

[a] *Division of Fluid Dynamics, Department of Mechanics and Maritime Sciences, Chalmers University of Technology, Göteborg 41296, Sweden*
[b] *Corresponding author: maggiolo@chalmers.se, Tel: +46 031 772 1398*

Abstract

Fouling on heat exchanger surfaces significantly impedes heat recovery from exhaust gases in many industrial applications. An introduction of the process of self-cleaning possibly represents an efficient solution to this well-known problem. Even if special treatments of the surfaces can help to protect them from fouling, it is still not well understood how to properly design heat exchangers in order to promote the self-cleaning process. In the present study, we investigate by means of Lattice-Boltzmann-based simulations the pivotal role of two-phase flow patterns and condensation-related phenomena in understanding the mechanisms that promote the self-cleaning, and, consequently, a stable heat recovery. In particular, we identify optimal flow conditions and two-phase flow characteristics that allow a clean and efficient operation of compact heat exchangers. Our results indicate that low heat duties and flow rates, which induce the condensation of small and motile droplets able to collect gas impurities, are beneficial for provoking and sustaining self-cleaning mechanisms. We therefore suggest that an effective design of self-cleaning heat exchangers should primarily be governed by principles of two-phase flow, rather than by the heat transfer duty. This work thus represents a step forward in identifying and proposing a procedure for an optimal design of heat exchangers to facilitate an effective heat recovery process from a wider range of exhaust gas mixtures.

Keywords: self-cleaning, heat recovery, exhaust gases, two-phase flows, dropwise condensation

1. Introduction

Compact heat exchangers that involve the cooling of a condensible mixture are found in a broad variety of industrial applications, e.g. in metallurgic furnaces, diesel or coal power plants and biomass gasifiers. In particular, compact heat exchangers play a significant role in the exhaust gas waste heat recovery (Alfa-Laval, 2018, Shi et al., 2011, Kilkovsky et al., 2014). In combustion chambers, a great amount of energy is usually converted into thermal energy, so that the total energy efficiency of the process depends on the heat recovery effectiveness during gas cooling. The possibility of recovering heat during the cooling of the exhaust gases is an enticing prospect in order to increase the efficiency and decrease the environmental impact of such technologies.

Heat recovery is however significantly limited by fouling, a phenomenon that involves the condensation of heavy hydrocarbons, collectively known as tar (Rabou et al., 2009), present in the gas. The flowing gas deposits these condensed organic compounds onto filters, pipe surfaces and other parts of the equipment, which thereby need an expensive and constant cleaning maintenance (Li et al., 2017, Melo et al., 2012). Fouling affects also heat exchanger surfaces, significantly impeding their application for waste heat recovery. The economical impact and cost of fouling on heat exchangers has been quantified as 2.5% of the industrialised nations GDP (Müller-Steinhagen et al., 2005). Furthermore, fouling is considered responsible for $1 \div 2.5\%$ of the global anthropogenic emissions of CO_2 (Müller-Steinhagen et al., 2009).

Recent technological advancements in material science have opened a route for anti-fouling surfaces through the application of specific coatings. Even though their practical applications are still at an early stage, such anti-fouling surfaces are nowadays studied for a variety of applications, for instance, when preventing corrosion and fouling in marine environments (Banerjee et al., 2011).

In a recent experimental study, we have revealed the possibility of producing anti-fouling surfaces for compact heat exchangers and allowing exhaust gas heat recovery (Maggiolo et al., 2018). These functional surfaces have been coated in order to induce a self-cleaning mechanism that limits the hydrocarbon adhesion to the surfaces. The coating process of the heat exchanger surfaces involved a hydrophobical treatment of the corrugated plates, which has allowed to achieve a contact angle of $\sim 90^\circ$ and to promote dropwise condensation. The coated plates showed a promising fouling-resistant be-

haviour when applied to a heat exchanger used for the cooling of the gas produced during biomass gasification. The process of biomass gasification is known to produce an exhaust gas extremely rich in hydrocarbons and, consequently, to be heavily subjected to tar fouling (Larsson et al., 2013, Thunman et al., 2018). The interaction between the tar hydrocarbons, the condensed water vapour present in the the gas mixture, and the coated surfaces has been found critical for achieving anti-fouling mechanisms. Our experiment disclosed that an efficient self-cleaning effect is triggered by the formation of small and uniformly distributed condensed water droplets, which are able to collect tar and protect the heat exchanger surfaces. In particular, it has been noted that dropwise condensation is a favourable condition for achieving a self-cleaning mechanism, since the former mechanism is, in comparison with a filmwise one, characterised by a higher liquid surface area available for collecting gas impurities. On the contrary, the protection of the corrugated surfaces provided by a continuous liquid film formation has been found difficult to realize in practice. Fig. 1 reports pictures from our experiment with coated and uncoated plates and a sketch of the heat and mass transfer processes and the corresponding relevant length scales in the heat exchanger.

Undoubtedly, the potential application of self-cleaning heat exchangers that are able to resist fouling and thereby to stably recover heat, is an exciting and intriguing perspective in all cooling processes involving a hydrocarbon-rich exhaust gas. However, detailed information is needed on the water condensation phenomena in compact heat exchangers in order to achieve the desired self-cleaning effect under different operative conditions.

The usual practice for designing heat exchangers entails that their main features, such as type, geometry, dimensions and number of plates, are defined on the basis of specific requirements for the intended application. This practice, for instance, includes the dimensioning of the heat exchanger at a fixed heat duty and pump power or length of the heat exchanger (Webb, 1981). In applications where tar fouling is believed to be an important limiting factor, it is the norm to treat the gas before entering the heat exchanger with special filters or to try to tune the operative parameters in the process in order to obtain a cleaner gas and avoid fouling.

In the present study, we propose a different approach: to design the heat exchanger in such a way to achieve the optimal fluid-dynamic and thermodynamic conditions that promote the self-cleaning effects on the heat exchanger surfaces. To this end, we have to comprehend and characterise the two-phase flow patterns during dropwise and filmwise condensation. Also, we need to

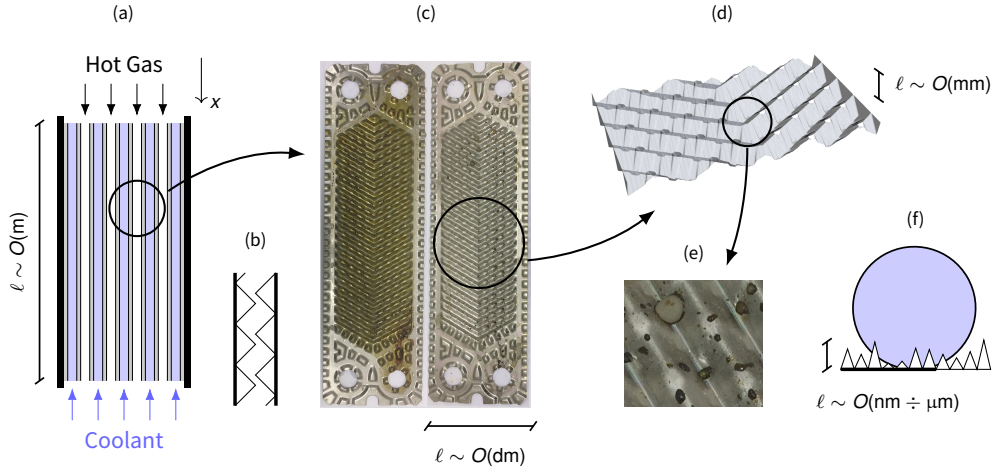

Figure 1: Schematic of a heat exchanger for exhaust gas heat recovery and information from our previous experimental study (Maggiolo et al., 2018). Note that in addition to the pictures, the fluid-dynamic length scales are given characterising the main heat and mass transfer phenomena. (a) sketch of a compact heat exchanger with parallel plates; (b) sketch of a cross-section of two sandwiched corrugated plates; (c) from the actual experiment: tar fouling on an uncoated plate after 2 hours of operation (left) and self-cleaning effect on a coated plate (right); (d) a fishbone-like structure as a part of the corrugated plate; (e) from the actual experiment: dropwise condensation on ribs and valleys; (f) sketch of a condensed droplet over a nanostructured surface.

investigate the droplets mobility and coalescence, and their dependence on the main heat and mass transfer phenomena. Ideally, the heat exchanger should be operated in such a way to induce a large enough number of small and evenly distributed water droplets, that can uniformly collect tar and promote self-cleaning. In this regard, numerical simulations can become a suitable tool to substitute an expensive experimental campaign and identify the operative conditions, the heat duty and the pump power required for an optimal and clean operation of the heat exchanger.

Numerous studies have been devoted to the investigation of dropwise condensation on superhydrophobic nano-structured surfaces of heat exchangers (Rose, 1967, Miljkovic and Wang, 2013, Cho et al., 2017). The chemical and structural composition of the surfaces at the nanoscale is known to affect the small-sized droplet shape and detachment mechanisms. To study such phenomena by numerical simulations, the smallest and largest physical length scales must be resolved, from nano- to millimetres (see Fig. 1 for a schematic

picture of the different length scales characterising the phenomena). To simulate just one single droplet can be computationally expensive. A simulation at the nanoscale of several droplets condensing on a heat exchanger surface some 10 centimetres long is computationally prohibitive.

Therefore, in order to investigate the spatial distribution of dropwise and filmwise condensation under different heat exchanger operating conditions, we limit our analysis to the microscale, while the characterisation of the nanostructured surfaces is out of the scope of this study. During dropwise condensation, the droplets size depends mostly on the maximum size for the droplet growth and on coalescence phenomena (Weisensee et al., 2017). The droplet size is expected to be greatly affected by the surface geometrical structure, in particular in compact heat exchangers where the typical geometrical lengths are defined by the corrugated surface structure (see e.g. Fig. 1e). The present analysis therefore concerns the collective behaviour of condensing droplets that is mainly determined by the heat, mass and momentum transfer mechanisms and by the geometry of the corrugated surface at the microscale.

In Section 2 the numerical methodology is presented, whereas the main results are presented in Section 3 and their significance for practical applications discussed in Section 4.

2. Numerical Methodology

The compact heat exchangers used in gas waste heat recovery are typically characterised by a corrugated fishbone-like surface structure, where the gas to be cooled and the cooling fluid flow in opposite directions. The plates are also sandwiched in the opposite direction, so that fluids are forced to flow along a very complex network of microchannels. This particular configuration is designed to maximise the heat transfer and minimise dead regions. In the present study, we reconstruct the typical geometry of a compact heat exchanger used for exhaust gas waste heat recovery in order to study the two-phase flow behaviour during vapour condensation (Alfa-Laval, 2018). We consider a part of the heat exchanger: two plates of width 8 cm and length 4 cm. The height of the plate corrugations is 5 mm so that, when they are sandwiched, their total height is 1 cm. The geometrical reconstruction of the plates is represented in a regular lattice grid that will be used later as an input for two-phase flow simulations. The overall domain size is composed

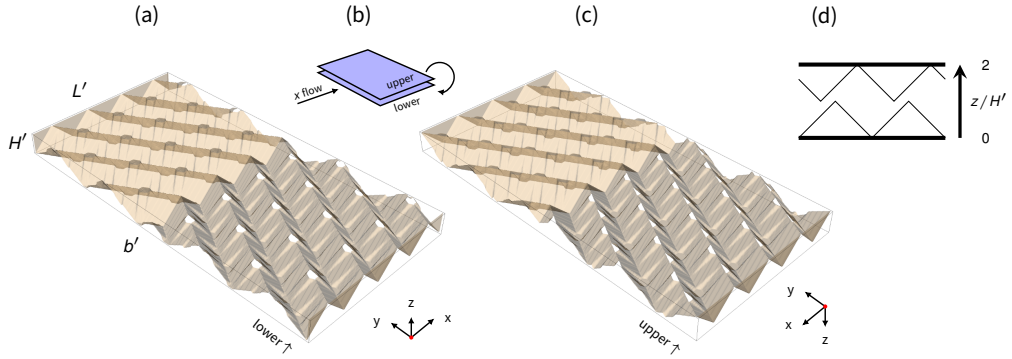

Figure 2: Three-dimensionalreconstruction of the heat exchanger plates and the simulation domain. The surfaces are characterised by fishbone-like structures: one along the flow direction (a) and the other one opposite to the flow direction (c). Inside the heat exchanger, they are sandwiched (b). A sketch of a cross-section is represented in (d). The flow is forced along the x direction by a body force representing an equivalent pressure gradient.

of $(L' \times b' \times 2H')$ computational cells, where $L' = 240$, $b' = 480$ and $H' = 30$, see Fig. 2.

A three-dimensional D3Q19 Lattice-Boltzmann model has been used for simulating the flow. The two-phase flow, based on the Shan-and-Chen framework (Shan and Chen, 1993), has been solved together with the temperature field by means of a two-way coupling approach, in order to accurately simulate condensation phenomena and to obtain a consistent thermodynamic description of the latent heat. The Lattice-Boltzmann equations for the flow and temperature are (Succi, 2001, Yuan and Schaefer, 2006):

$$f_r(\boldsymbol{x} + \boldsymbol{c}_r\delta t, t + \delta t) - f_r(\boldsymbol{x}, t) = -\tau^{-1}(f_r(\boldsymbol{x}, t) - f_r^{eq}(\boldsymbol{x}, t)) + F_r \quad (1)$$

$$g_r(\boldsymbol{x} + \boldsymbol{c}_r\delta t, t + \delta t) - g_r(\boldsymbol{x}, t) = -\tau^{-1}(g_r(\boldsymbol{x}, t) - g_r^{eq}(\boldsymbol{x}, t)) \quad (2)$$

where $f_r(\boldsymbol{x}, t)$ and $g_r(\boldsymbol{x}, t)$ are the flow and temperature distribution functions at the position $\boldsymbol{x}$ and time t along the r-th direction; $\boldsymbol{c}_r$ is the so-called discrete velocity vector along the r-th direction, $\tau = 1$ is the relaxation time which provides a direct link to fluid viscosity and thermal diffusivity (Prandtl number is unity), and f_r^{eq} and g_r^{eq} are the flow and temperature equilibrium distribution functions along the r-th direction. F_r is the body force acting on the fluid. The first equation (Eq. 1) represents the fluid flow at the mesoscale; its macroscopic counterpart is the momentum equation. The second equation

(Eq. 2) represents the temperature field and its macroscopic counterpart is the energy equation in the hypothesis of negligible viscous heat dissipation (as usually assumed in the presence of low-velocity flows, that is, for low Brinkman numbers). The macroscopic variables $(\rho, \boldsymbol{u}, T)$ and are deduced from the hydrodynamic moments:

$$\rho = \sum_r f_r \tag{3}$$

$$\rho \boldsymbol{u} = \sum_r \boldsymbol{c}_r f_r + \frac{1}{2}\left(\frac{\Delta P}{L} + F_{sc}\right) \tag{4}$$

$$T = \sum_r g_r \tag{5}$$

where F_{sc} is the Shan-Chen gas-liquid interaction force. (Shan and Chen, 1993) The fluid is forced along the streamwise direction x by a body force which mimics the effect of the pressure gradient $\Delta P/L$. The forcing scheme adopted here is the one described in detail by Guo *et al.* (Guo et al., 2002). Following this approach, the body force in Eq. 1 is defined as:

$$F_r = \left(1 - \frac{1}{2\tau}\right) w_r \left(\frac{\boldsymbol{c}_r - \boldsymbol{u}}{c_s^2} + \frac{\boldsymbol{c}_r \boldsymbol{u}}{c_s^4}\boldsymbol{c}_r\right) \frac{\Delta P}{L} \tag{6}$$

with c_s representing the speed of sound and w_r the D3Q19 weight parameter (Succi, 2001). The two-way fluid-temperature coupling is ensured through a proper modification of the fluid equilibrium distribution function (Zhang and Tian, 2008). The fluid and temperature equilibrium functions are thus defined as:

$$f_r^{eq} = w_r \rho \left(\frac{1 - 2T}{c_s^2} - \frac{\boldsymbol{u}_{eq}^2}{2c_s^2}\right), \; r = 1 \tag{7}$$

$$f_r^{eq} = w_r \rho \left(\frac{T}{c_s^2} + \frac{\boldsymbol{c}_r \boldsymbol{u}_{eq}}{c_s^2} + \frac{(\boldsymbol{c}_r \boldsymbol{u}_{eq})^2}{c_s^4} - \frac{\boldsymbol{u}_{eq}^2}{2c_s^2}\right), \; r = 2 - 19 \tag{8}$$

$$g_r^{eq} = w_r T \left(1 + \frac{\boldsymbol{c}_r \boldsymbol{u}}{c_s^2} + \frac{(\boldsymbol{c}_r \boldsymbol{u})^2}{c_s^4} - \frac{\boldsymbol{u}^2}{2c_s^2}\right) \tag{9}$$

where the equilibrium velocity in Eqs. 7 and 8 is defined as $\boldsymbol{u}_{eq} = \boldsymbol{u} + (\tau - 1/2)F_{sc}$. A non-ideal equation of state thus provides the thermodynamic link between the two-phase density of the fluid ρ and temperature T (Zhang and

Tian, 2008):

$$P = \rho T + \frac{G}{2} c_s^2 \, \Psi^2 \tag{10}$$

with P being the pressure and G the Shan-Chen parameter directly related to the two-phase surface tension, here set as $G = -9.5$. The moving gas-liquid contact line is characterised by an equilibrium contact angle of 90° which is implemented through a proper averaging of the density-dependent function $\Psi = e^{-1/\rho}$ in the vicinity of the three-phase contact point (De Maio et al., 2011):

$$\Psi_{wall} = N^{-1} \sum_{N} \Psi + \Delta_w \tag{11}$$

where Ψ is the density-dependent dependent function mimicking the Van-der-Waals intermolecular force at the solid wall (Ψ_{wall}) and in the nearest fluid computational nodes N. By tuning the parameter Δ_w, it is possible to represent different contact angles at the macroscopic scale. An example of the influence of the Lattice-Boltzmann parameter on the contact angle is provided in Fig. 3. It should be noted that the specific form of the density-dependent function Ψ used here ensures thermodynamc consistency (Sbragaglia and Shan, 2011). A Lattice-Boltzmann study which describes a similar two-phase thermodynamic coupling can be found in Biferale *et al.* (Biferale et al., 2012).

2.1. Validation of the numerical model

In the Shan-and-Chen Lattice-Boltzmann framework, condensation and the release of the latent heat occur at proper thermodynamic conditions, provided that a small perturbation is introduced in the system. In the present simulations, the velocity and the temperature gradients induced by the geometric corrugations and the heat transfer at the plates of the heat exchanger are able to provoke such a perturbation, thereby inducing condensation. The latent heat is not a quantity known *a priori*, but it implicitly depends on the thermodynamic parameters of the numerical model. To validate the model and quantify the latent heat, we have simulated the one-dimensional Stefan problem that describes a condensing front induced by surface cooling (Gupta, 2017). In the classical Stefan problem, the time-dependent behaviour of the growth of the liquid front is determined by the Jakob number (also termed

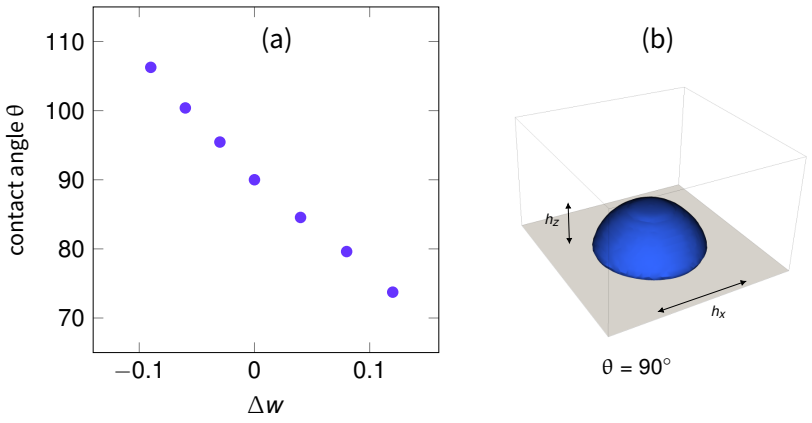

Figure 3: (a) The dependence of the contact angle θ on the numerical parameter Δw. (b) A droplet of one millimiter-diameter over a surface with $\Delta w = 0$ subjected to gravity. The contact angle is determined as $\theta = 2\ \tan^{-1}(2h_z/h_x) = 90°$.

the Stefan number). It is defined as the ratio between the sensible and the latent heat:

$$Ja = \frac{c_p\ \Delta T_0}{\lambda}\ , \tag{12}$$

where c_p is the specific heat, λ is the latent heat and ΔT_0 is a reference temperature difference (for instance, in the Stefan problem that difference is usually defined as the one between the saturation and the cooling temperatures). The growth of the thickness of the condensed fluid $\delta(t)$ is compared to the first-order approximation of the Neumann analytical solution, for which (Charach et al., 1988):

$$\delta(t) \sim 2\alpha\ Ja \int \Theta_i(t)\ dt\ . \tag{13}$$

where $\Theta_i(t)$ is the non-dimensional difference between gas-liquid interface temperature $T_i(t)$ and the cooling temperature T_w, i.e. $\Theta_i = (T_i(t) - T_w)/\Delta T_0$, and α is the thermal diffusivity. In the present validation case, we have set $Ja \sim 1$. The numerical results match the analytical solution well, with a constant latent heat of $\lambda = 0.68$ (in Lattice-Boltzmann units), as represented in Fig. 4. Furthermore, we have compared the value of the latent heat obtained from the one-dimensional Stefan problem, with the value obtained from the simulation of static three-dimensional droplets at different thermodynamic

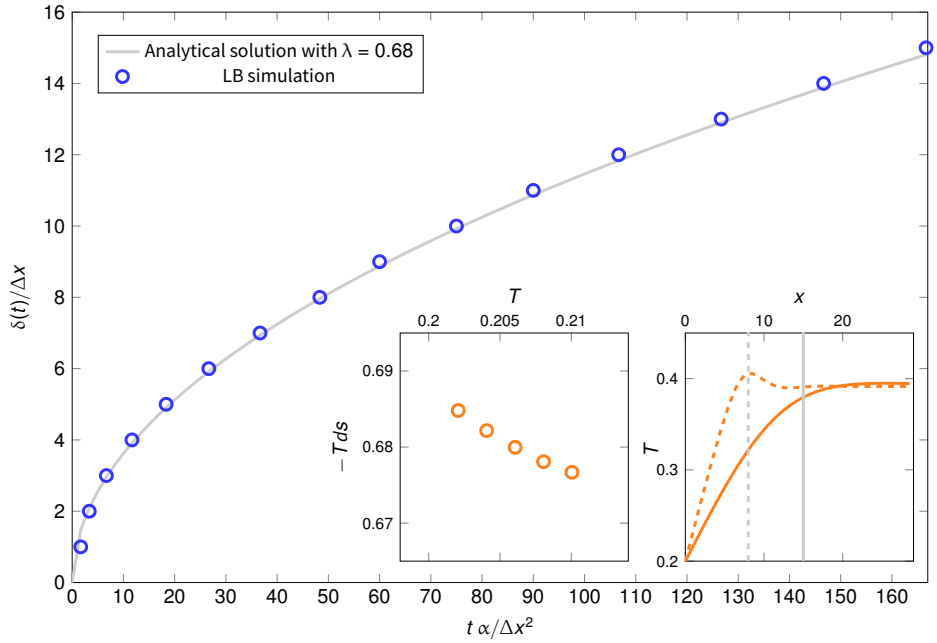

Figure 4: One-dimensional Stefan problem: a condensing liquid front induced by surface cooling. The cooled surface is placed at $x = 0$. Main plot: comparison between numerical solution for the time-dependent liquid front thickness $\delta(t)$ and the approximated analytical Neumann solution (Charach et al., 1988). Time and front thickness have been normalised with the lattice unit cell, Δx, and the thermal diffusivity, α. Left inset: variation of latent heat $\lambda = -T\ ds$ with temperature T computed from three-dimensional simulations of static liquid droplets immersed in a gas phase. Right inset: Temperature profile at $t\alpha/\Delta x^2 = 167$ for the validation case with equal densities of the two phases (solid line) and in the case of significantly different densities (dashed lines) that induces an extra convection mechanism.

equilibria (i.e. at different temperatures) (Biferale et al., 2012). From the latter, as expected and depicted in the left inset of Fig. 4, we extract the exact same value so that we can conclude that the model is correctly simulating the heat released during condensation. The robustness of the present model, theoretically asserted in previous works (Sbragaglia and Shan, 2011), is thus further confirmed by the direct relation between latent heat λ and variation of the specific entropy $s = -log(\rho/T^{3/2})$ (Biferale et al., 2013).

It should be noted that, in order to model the one-dimensional Stefan problem, we have set similar properties of the two fluids (i.e. densities and viscosities of the phases are similar and their thermal diffusivities equal).

Consequently, the effect of the gas phase behaviour on the condensing liquid front has been considered negligible. When the physical properties of the phases differ, the Neumann analytical solution of the Stefan problem (Eq. 13) is no longer valid. For instance, when densities differ appreciably, a convection mechanism is triggered at the liquid-gas interface caused by the sudden change of density of the condensed fluid (Chambre, 1956, Gupta, 2017). As a consequence, the growth of the liquid front is slowed down and the heat flux at the interface is increased, as highlighted in the right inset of Fig. 4. When the liquid-gas interaction at the interface is further enhanced by a gas flowing in the direction perpendicular to the liquid front growth and the viscosities of the phases differ, such as in a heat exchanger application, the growth mechanism becomes even more complex. In this situation, the mass transfer in the liquid film has to be taken into account (as is the case in the classic Nusselt filmwise condensation theory), the liquid-gas interface can be deformed under shear flow, and heat can be transported away from the interface via convection. Therefore, we expect the mechanisms of droplet growth, droplet transport and heat transfer on heat exchanger surfaces to be affected not only by the Ja number, but also by a non-dimensional number that quantifies the contribution of the moving fluid. In what follows, we will investigate and discuss this argumentation; the viscous flow contribution of the gas phase will be quantified by the capillary number Ca, which we expect to affect the liquid-gas two-phase relative mobility.

2.2. Set-up of the numerical simulations

The condensation mechanisms over heat exchanger plates play a pivotal role for determining the effectiveness of the self-cleaning effects of the surfaces. Such mechanisms comprise heat transfer from the fluid to the cooling plates, liquid droplets and/or film formation and growth, two-phase flow patterns and coalescence. In order to study these complex and interdependent phenomena, a part of the whole heat exchanger is simulated, as represented in Fig. 2. The chosen domain size is sufficiently large to capture the largest relevant fluid-dynamic length scale (which is of the order of the height of plate corrugation) and sufficiently small to allow computational efficiency.

Even though the model is not able to simulate large density ratios due to numerical instabilities, we are able to analyse a two-phase flow system characterised by a dynamic viscosity ratio of $M \sim 35$ — a representative value for a water-vapour system at the relevant conditions. In two-phase flows where the surface tension dominates (i.e. for low capillary numbers) and the

characteristic velocity and length scales of the flow are small (i.e. for low Reynolds numbers), the two-phase flow behaviour is determined by the dynamic viscosity ratio, rather than the density ratio (Vizika et al., 1994, Odeh, 1959, Chibbaro, 2008). Since we are interested in low-velocity exhaust gas flows as in our previous experiment (Maggiolo et al., 2018), the simulations correctly represent a water-vapour system for this particular application. A single-component two-phase system is considered, therefore the density and viscosity ratios are equal. It should be also noted that previous simulations matched well the aforementioned experimental results, further confirming the robustness of the model. For a comparison between numerical simulations and experimental analyses, the reader is referred to Maggiolo *et al.* (Maggiolo et al., 2018).

A fluid with an initial temperature $T_0 \leq T_{sat}$ in a metastable thermodynamic state, flows between the heat exchanger surfaces. The flow is induced by the applied pressure gradient $\Delta P/L$. Periodic boundary conditions are imposed at the inlet and outlet of the domain and no-slip velocity conditions are imposed at the fluid-solid boundaries, via a half-way bounce-back algorithm (Succi, 2001). The heat exchanger surfaces are cooled at a temperature $T_w < T_0$ so that a preset amount of fluid $n^* = 10\%$ condenses — a reasonable value when dealing with exhaust gas mixture produced by biomass gasification (Thunman et al., 2018). The liquid and gas phases after condensation reach thermodynamic equilibrium. The plates are kept at a constant temperature T_w, in order to mimic the heat transfer phenomena that have taken place during our previous experiment: in the experiment, the plates were in contact on the external side with a cooling liquid characterised by a mass-flow rate a thousand times higher than that of the fluid to be cooled. The latter observation implies that in numerical simulations we can safely neglect variations of the plate temperatures.

In the limit of infinite time, the gas would reach the temperature of the plates and all the heat would be extracted. For computational reasons, the simulations are stopped after a certain time ($t_1^* = 0.7$) at which all the pre-established amount of fluid has condensed and the flow is well developed (i.e. the residual of the Re number is less than 10^{-4}). The simulation time t has been normalised with the characteristic viscous time of the flow $t_c = 4H'^2/\nu$, so that $t^* = t/t_c$, where H' is the average height of the flow cross sectional area and $2H'$ the equivalent hydraulic diameter for a two-dimensional channel of height H'. For the sake of clarity, the non dimensional time t_1^* corresponds to $t_1 = t_1^*\ t_c \sim 0.7\ (1\ \mathrm{cm}^2)/(10^{-5}\ \mathrm{m}^2/\mathrm{s}) \sim 7$ s in real units, if one considers

the fluid as saturated steam. Without loss of generality, variables can be determined in real units by means of the corresponding dimensionless parameter. For instance, the fluid velocity can be calculated by means of the capillary number as U_{real} (m/s) = Ca σ(N/m)/μ (kg/ms). The simulations are performed at a Prandtl number of unity, so that the characteristic time of thermal diffusion is the same as t_c. The mean temperature of the two-phase system at the final time t_1^* is denoted T_1, a value which results very close to that of the cooled surfaces T_w.

To simulate different possible operating conditions of a heat exchanger applied to the cooling of an exhaust gas, we perform six simulations by varying the value of the Jakob number as $Ja \sim 10^{-2}$, 10^{-1} and 1 and the capillary number as $Ca \sim 10^{-4}$ and 10^{-2}. We define the Jakob number as in Eq. 12 with the reference temperature difference $\Delta T_0 = T_0 - T_1$ so that it becomes directly related to the heat exchanger heat duty $T_0 - T_w \sim \Delta T_0$. The different capillary numbers result instead from the variation of the fluid forcing, which directly affects the mean fluid velocity U and the shear rate $\dot{\gamma} \sim 2U/\ell_c = U/H'$. Thus, we define the capillary number as the ratio between the flow viscous shear rate and the droplet surface tension forces:

$$Ca = \frac{\mu \dot{\gamma}\ h_{drop}}{\sigma} = \frac{\mu U}{\sigma}, \tag{14}$$

with μ the dynamic viscosity of the gas phase and σ the liquid-gas surface tension. We set the characteristic height of the droplet subjected to the flow as $h_{drop} \sim H'$. Expression 14 conveys important information about the transport mechanism of sliding droplets attached to solid surfaces and it is therefore fundamental for characterizing the self-cleaning effects (Li and Pozrikidis, 1996, Schleizer and Bonnecaze, 1999).

3. Results

3.1. Fluid cooling

The results of our numerical simulations show that the gas cooling process differs on the basis of the Jakob number. Figure 5 highlights this dependence. In order to quantify the heat transfer mechanism, in Fig. 5 the time-dependent non-dimensional heat duty is represented:

$$\Theta(t) = (\langle T(t) \rangle - T_1)/\Delta T_0\ , \tag{15}$$

where $\langle T(t) \rangle$ is the spatially averaged temperature at the time t and $\langle \cdot \rangle$ indicates the spatial averaging operator over the entire fluid domain. The heat duty does not decrease linearly. Instead, as shown in Fig. 5, the mean fluid temperature is characterised by significant fluctuations which highlight a periodic redistribution of the heat, to or from the cooling plates in the form of sensible heat, and to or from the liquid phase in form of latent heat. In fact, along with the dominant phenomenon of fluid cooling, we also observe temporary inversions of the heat flux from the plates to the fluid in large regions where the fluid is subcooled, i.e. where $T < T_w$, together with adsorption or release of latent heat in the regions where liquid evaporates or condenses. This unsteady behaviour induces the observed thermal fluctuations.

A clear trend in the cooling process, which depends on the Ja number, is shown on Fig. 5. The cooling is fast in the case of $Ja \sim 1$ and the majority of the total heat ΔT_0 is transferred to the plates at short times. On the contrary, when $Ja < 1$ the cooling is slowed down. We stress here that the amount of the condensing liquid is the same in all the simulations. Also, since the flow is laminar, the heat transfer coefficient is expected to vary only slightly. The computation of the heat transfer coefficient is not trivial in this three-dimensional geometry; one should take into account the three-dimensional structure of the temperature and flow fields, and make a proper choice of the bulk temperature in order to compute the Nusselt number, see e.g. (Metwally and Manglik, 2004). A rough estimation of the Nusselt number has been done by approximating the flow as single-phase and two-dimensional, with the characteristic length determined by the hydraulic diameter $2H'$, and by considering the temperature gradients only along the vertical direction z; then, by averaging the Nusselt number values among all the considered cases with varying Ja and Ca. This computation leads to $Nu = 8.25 \pm 1.34$ (where 1.34 is the standard deviation), a value very close to the analytical one for a laminar fully-developed two-dimensional channel flow with constant axial heat flux (which is here induced by the periodic boundary conditions along x) and wall temperature, i.e. $Nu = 8.235$ (Kays et al., 2005).

We hence argue that it is not the reduction of the heat transfer coefficient that induces the increase of the cooling time. Instead, we ascribe this behaviour to the significant contribution needed to heat up the system and given by the latent heat. In other words, when the latent heat is dominant, the system takes more time to be cooled down, since the heat that is uniformly released during condensation significantly increases the effective heat

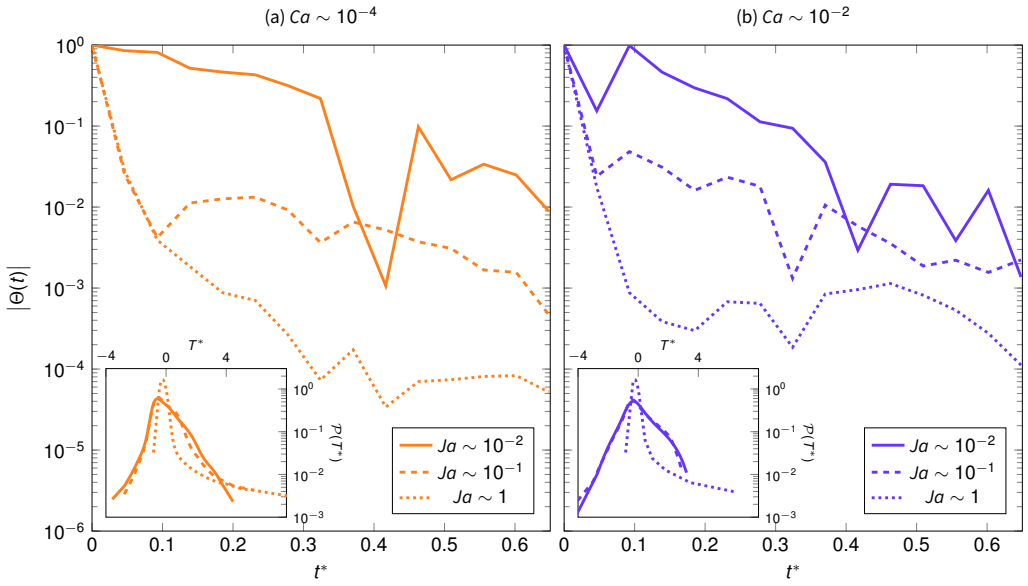

Figure 5: Time-dependent behaviour of the non-dimensional heat duty $\Theta(t)$ for (a) $Ca \sim 10^{-4}$ and (b) $Ca \sim 10^{-2}$ with varying the Ja number. The time taken to cool down the fluid is qualitatively higher for $Ja < 1$, that is when the latent heat is significantly higher than the sensible heat. Insets: Probability Distribution Functions $\mathcal{P}$ of the normalised temperature $T^* = (T - \langle T \rangle)/\sigma(T)$, where $\sigma(T)$ is the variance, at $t^* = 0.05$.

duty of the system. The non dimensional effective heat duty can be quantified as $\Theta_{eff} \sim 1 + Ja^{-1}$ and it results in $\Theta_{eff} = 2$ when $Ja \sim 1$, whereas $\Theta_{eff} \sim 101$ when $Ja \sim 10^{-2}$.

The Ja number also affects the temperature distribution in the flow. The insets of Fig. 5 show the probability distribution functions (PDF) of the temperature flow fields at short time $t^* = 0.05$. All PDFs are characterised by a highly non-Gaussian shape with a sharp peak denoting that a great amount of the computed temperatures are close to the mean value, which we note is very close to the wall temperature T_w. When $Ja \sim 1$, the PDF significantly shrinks and presents a long tail on the right-hand side, indicating that almost all the fluid has a temperature close to the mean one, but also that the deviations from it are not so rare. This result is consistent with the previous observation that, with the Jakob number equal to unity, the majority of the heat is transferred to the plates very fast, but in some places the fluid remains particularly warm, with a temperature close to the initial one. By varying the capillary number Ca, we observe no significant variation

in the behaviour of the fluid cooling.

From the results of the cooling process, we note that, under the considered thermodynamic conditions, the heat exchanger is over-dimensioned on the basis of the conventional design practice. In fact, the fluid temperature reaches a value close to the wall temperature in a few seconds, or, equivalently, the thermal boundary layer develops in a few centimetres, in all the considered cases. By looking at the effective heat duty of the system rather than at the temperatures in absolute terms, we observe a slower cooling process in the case when the initial temperature is close to the wall temperature. In the latter case, the over-dimensioning of the heat exchanger is dramatic. The question of how the over-sizing of the heat exchanger can affect the two-phase flow pattern formation during condensation and how it can possibly induce a better self-cleaning mechanism, is thus discussed in the following subsection.

3.2. Liquid condensation and two-phase flow patterns

Liquid condensation happens at short times. We can qualitatively estimate the time required to condense the liquid percentage n^* from Eq. 13, by assuming an equivalent filmwise condensation process in a static fluid between two parallel plates with a linear decrease of temperature Θ_i, so that $\int \theta_i \, dt \sim t/2$. The liquid percentage is then computed as $n^* \sim \delta/\ell_c$, where $\ell_c = 2H'$ is the equivalent hydraulic diameter, and the characteristic time for condensing n^* yields $t^*_\delta \sim n^{*2}/Ja$. Figure 6 shows the time-dependent condensation process for all the considered cases. The growth behaviour is not merely following a power law $t^{*1/2}$ as predicted by Eq. 13. This result is not surprising since the growth mechanism is more complicated than the simple one predicted for a static fluid between two parallel plates. Even though the condensation behaviour in time completely differs from the solution of the Stefan problem, the time required to condense $n^* = 0.1$ at $Ja \sim 1$ can be correctly estimated with the aforementioned approximation, that is $t^* \sim 0.01 \sim t^*_\delta$. However, for smaller Jakob numbers, the same approximation is no longer valid. At very short times, we observe that with $Ja \ll 1$ the liquid growth is slightly slowed down, as highlighted in the insets of Fig. 6, but at longer times the liquid growth is significantly faster than the one predicted by Eq. 13.

In order to understand this unexpectedly fast growth at $Ja \ll 1$, we analyse the liquid spatial distribution along the wall-normal vertical direction z. Figure 7 depicts the liquid volumetric percentage $n_{xy}(z)$ computed along the

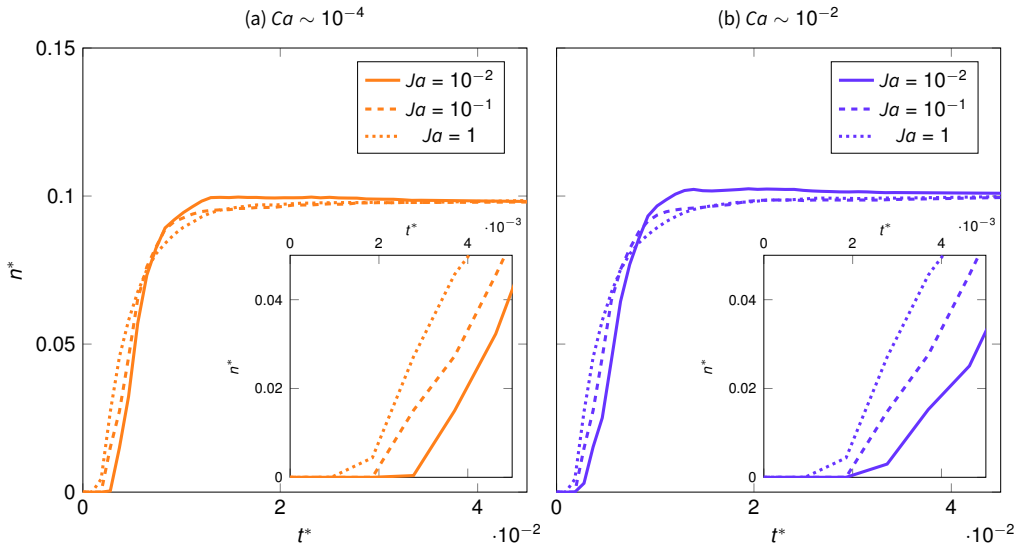

Figure 6: Ratio between the volume of liquid and the total fluid volume n^* against non-dimensional time t^*. This liquid volume percentage is plotted at different values of Ja and for (a) $Ca \sim 10^{-4}$ and (b) $Ca \sim 10^{-2}$. Insets: time-dependent behaviour of n^* at short times.

plane (x, y) at different times. When $Ja \sim 1$, the liquid tends to accumulate at the bottom and top of the domain, i.e. at $z/H' \to 0$ and $z/H' \to 2$. As a consequence, the behaviour of the liquid growth at $Ja \sim 1$ can resemble that of a filmwise condensation since the liquid tends to grow in the valleys of the heat exchanger, forming a continuous film, as in the classic Stefan problem. On the other hand, when $Ja \ll 1$ condensation occurs more likely dropwise in the centre of the fluid domain at $z/H' \sim 1$. A very low value of the Jakob number indicates that the sensible heat is much lower than the latent heat. For a water-vapour system $\lambda \sim 2\ 10^3$ kJ/kg and $c_p \sim 4$ kJ/kg, K. Therefore, by considering that the final temperature of the fluid in the heat exchanger is $T_1 \sim 20°$C, the initial temperature can be estimated as $T_0 \sim 25°$C for $Ja \sim 0.01$ and $T_0 \sim 70°$C for $Ja \sim 0.1$, meaning that the heat exchanger is operating well below the saturation conditions. Possibly, at very low Ja, droplets condense in the bulk fluid rather than close to the cooled plates and they then attach upon the heat exchanger ribs. This insight is confirmed in Fig. 7 and it also explains why condensation is occurring so fast at low Jakob numbers: indeed a dropwise growth rate is expected to be faster than a filmwise one, in particular in the presence of significant coalescence

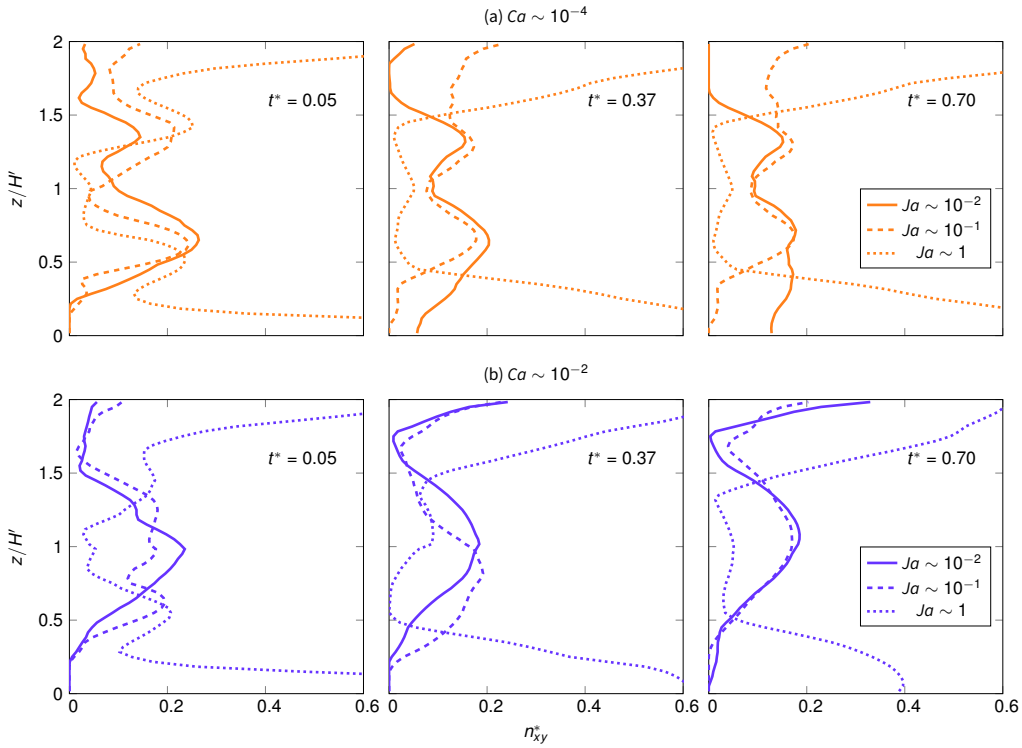

Figure 7: Percentage of liquid content n^*_{xy} along the non-dimensional vertical direction z/H'. The percentage n^*_{xy} is the averaged value along the plane (x, y), see Fig. 2 (d) for a sketch of the heat exchanger cross section. Profiles are shown for (a) $Ca \sim 10^{-4}$ and (b) $Ca \sim 10^{-2}$ with varying the Ja number at three different non-dimensional times $t^* = 0.05, 0.37$ and 0.70.

phenomena (Viovy et al., 1988, Leach et al., 2006).

From Fig. 7 we also observe that the effect of the capillary number on the liquid spatial distribution is substantial at $Ja \ll 1$, whereas it is negligible for $Ja \sim 1$. When the dropwise condensation occurs and droplets reside close to heat exchanger ribs, they can be transported more easily by the flow, having a higher velocity along the heat exchanger midplane $z/H' = 1$. The higher the effect of the flow shear rate over the capillary forces, i.e. the higher the capillary number, the more droplets are expected to deform and possibly slide along the surface (Li and Pozrikidis, 1996). This particular geometrical configuration of the heat exchanger, with alternate ribs and valleys, sustains droplets movement toward the midplane for the droplets attached to the bottom plate where the fishbone structure is aligned with flow. Instead, for

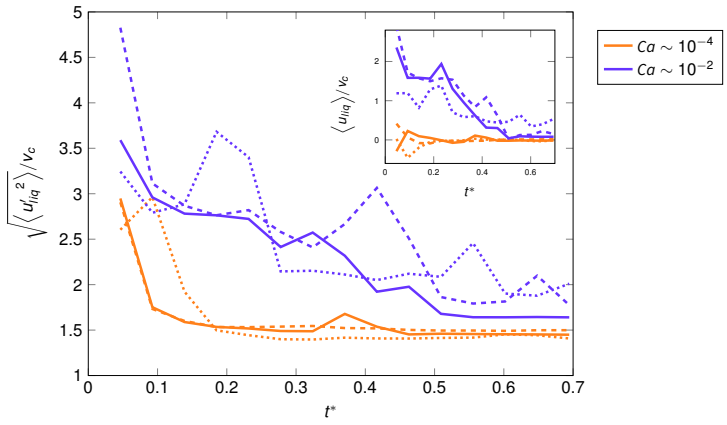

Figure 8: Streamwise liquid velocity fluctuations $(\langle u_{liq}'^2 \rangle)^{1/2}$ normalised with the characteristic velocity $v_c = \nu/H'$. The velocity fluctuations are plotted against non-dimensional time t^* for $Ja = 10^{-2}$ (solid lines), $Ja = 10^{-1}$ (dashed lines), and $Ja = 1$ (dotted lines), with varying the Ca number. Inset: non-dimensional streamwise mean liquid velocity $\langle u_{liq} \rangle$.

the droplets residing on the upper plate, the fluid forcing will contribute to push them to the top of the heat exchanger, as depicted in Fig. 7 at long non-dimensional times.

The effect of the capillary number Ca on the droplets mobility is also visible in Fig. 8, which represents the non-dimensional liquid velocity fluctuations in time. We deliberately chose to quantify the droplet mobility with the averaged streamwise velocity fluctuation since droplets can move in opposite directions in this complex geometry, and thus their mean velocity can appear extremely low, in particular at low capillary numbers (see the inset of Fig. 8). In any case, a very low mean velocity of a group of droplets does not imply that the droplets are not moving. Rather, it indicates that their displacements are counterbalanced since, for instance, some of them are moving forward and others back along the heat exchanger corrugated surface. Therefore, the droplet mobility can be better quantified by means of the non-dimensional velocity fluctuation:

$$u_{liq}'^{*} = \frac{\sqrt{\langle u_{liq}'^{\,2} \rangle}}{v_c} = \frac{1}{\nu/2H'} \left\langle \left(u_{liq} - \langle u_{liq} \rangle \right)^2 \right\rangle^{\frac{1}{2}} \tag{16}$$

where u_{liq} and $v_c = \nu/2H'$ are the liquid and the viscous characteristic velocities. When the capillary number is very low, the non-dimensional velocity

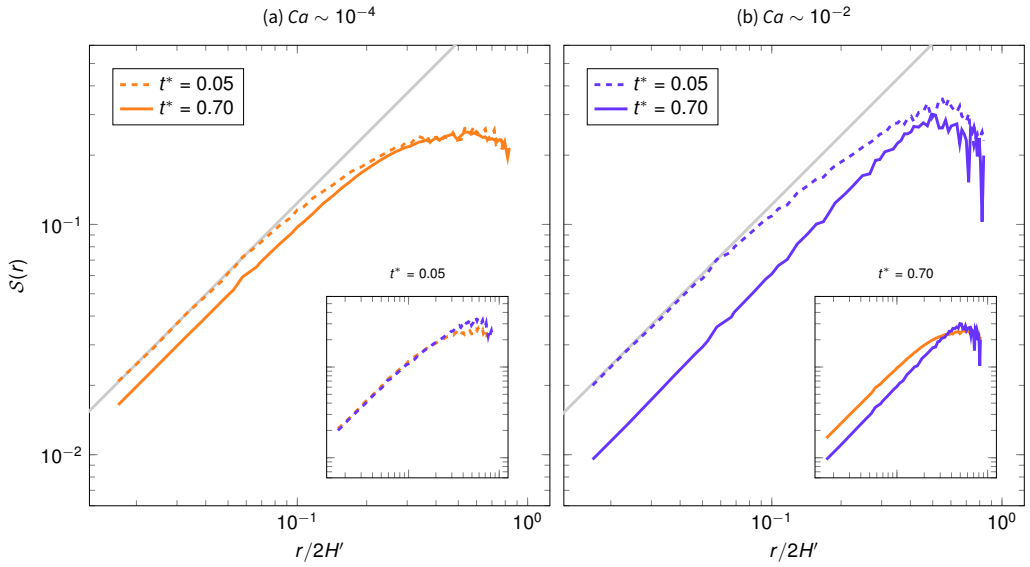

Figure 9: Spatial structure functions $\mathcal{S}(r)$ of the two-phase flow field for (a) $Ca \sim 10^{-4}$ and (b) $Ca \sim 10^{-2}$ at two different times: directly after condensation ($t^* = 0.05$, dashed lines) and at longer time ($t^* = 0.70$, solid lines). The slope coefficient of $\mathcal{S}(r)$ indicates the liquid-gas specific surface area whereas the change in the slope qualitatively addresses the mean droplet diameter on the corresponding x-coordinate. The grey line indicates $y = 1.24\ x$ in order to facilitate the comparison between the right and left panels. Insets: the structure functions for different Ca are compared at the same simulation time. Results are shown for $Ja = 10^{-1}$.

fluctuation diminishes rapidly to a value very close to unity. A qualitatively similar but slower behaviour is observed for higher Ca. The initial high velocities denote high droplets mobility sustained by a large temperature gradient, while at longer times droplets move more uniformly and they are subjected to velocity fluctuations governed by viscous forces. The described concept can be mathematically translated as: $u'^*_{liq} \rightarrow 1$ for $t^* \rightarrow 1$.

The time window for droplet motion is much longer for $Ca \sim 10^{-2}$, which we note is a value very close to the critical Capillary number $Ca_{cr} \sim 10^{-1}$ for advancing contact angles $\sim 90°$ (Li and Pozrikidis, 1996, Schleizer and Bonnecaze, 1999). When the value is close to the critical one, droplets are strongly deformed and they can eventually break up. Sliding fast on the surfaces, with highly deformed shapes, the droplets are more easily subjected to coalescence. In order to quantify coalescence, we compute the statistical distribution of liquid in the spatial domain through the spatial structure

function:

$$\mathcal{S}(r) = \left\langle \left(\bar{b}(x+r) - \bar{b}(x) \right)^2 \right\rangle , \tag{17}$$

where $\bar{b}(x)$ is the Boolean value corresponding to liquid (1) or gas (0) in the Cartesian position x, and r is the distance between the two points $x+r$ and x. The spatial structure functions convey two main pieces of information: (i) they decorrelate when r is greater than the mean droplet diameter d and (ii) their linear slope is proportianal to the droplets specific surface area (Blair et al., 1996). Figure 9 compares the structure functions for the two different capillary numbers and $Ja \sim 10^{-1}$. The results of these two cases can be extended to the cases with the Jakob number $Ja \sim 10^{-2}$, while for $Ja \sim 1$ (filmwise condensation) we observe a significantly lower specific surface area. For the comparison between condensation patterns obtained by numerical simulations and experimental data, at low capillary and Jakob numbers, the reader is referred to our previous work (Maggiolo et al., 2018). At short times, directly after the majority of water has condensed ($t^* = 0.05$), the spatial distribution of droplets is very similar for both cases. Instead, at longer times ($t^* = 0.7$) it differs significantly, as highlighted in the insets of Fig. 9. When the capillary number is low, the mean droplet size and the spatial distribution just slightly change: the mean droplet diameter and the specific surface area increase and decrease, respectively. We note that this behaviour indicates a small increase in the droplet diameter due to weak coalescence phenomena that consequently decrease the liquid-gas interfacial area. The same effect is dramatically enhanced with higher Ca, so that the final mean droplet diameter and the droplets specific surface area significantly increase and decrease, respectively. This discrepancy can be easily seen in Fig. 10 and in the zoom of snapshots in Fig. 11, which depicts the distribution of droplets in the heat exchanger at different times. High capillary numbers induce higher droplets mobility which eventually leads to significant coalescence phenomena and large liquid droplets, a phenomenon also easily discerned from the flow visualization in Fig. 12.

From this comprehensive picture that describes condensation, two-phase patterns, liquid mobility and coalescence, we deduce three main flow mechanisms taking place in our system: (i) at a finite Jakob number $Ja \sim 1$, condensation occurs in a filmwise fashion on the valleys of the heat exchanger plates. This is an undesired condition for achieving self-cleaning effects, since liquid water cannot easily be transported away and the amount of liquid sur-

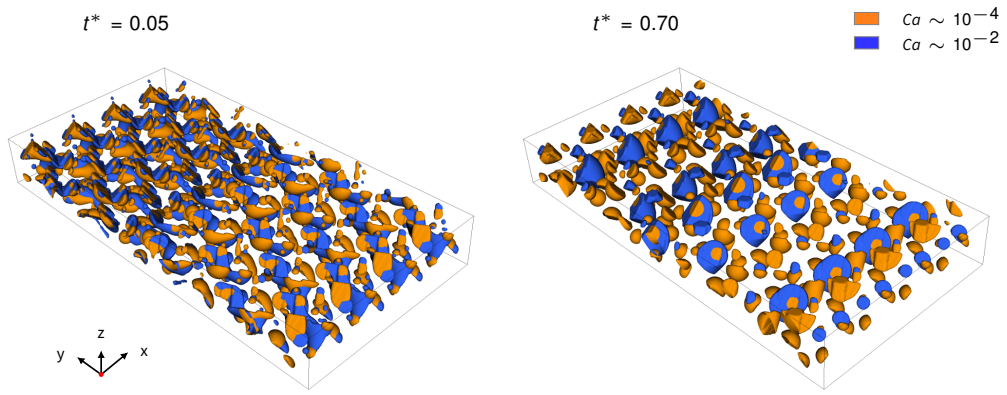

Figure 10: Snapshot of simulations representing the two-phase flow field at two different times: at short time directly after the majority of water had condensed, $t^* = 0.05$, and at longer time, $t^* = 0.70$. Isosurfaces are representing the liquid-gas surface areas for $Ca \sim 10^{-4}$ (orange) and $Ca \sim 10^{-2}$ (blue). The Jakob number is $Ja = 10^{-1}$.

face available for collecting gas impurities is low. Figure 13 clearly depicts the decrease of surace area at Jakob numbers around unity. Instead, at a Jakob number lower than unity, dropwise condensation occurs with the formation of liquid droplets mainly residing on the top of the ribs of the heat exchanger surfaces. When the capillary number is relatively high, close to a certain specific critical value ($Ca_{cr} \sim 10^{-1}$ for contact angle $\sim 90°$), (ii) droplets slide fast and merge easily together, leading to a successive formation of large drops — a two-phase spatial distribution that induces a decrease of the liquid surface area. This decrease is again well visible on Fig. 13, at a high capillary number. On the contrary, when the capillary number is lower (iii), the droplets move more slowly and preserve their initial shape. In this case, the two-phase spatial distribution is characterised by small and uniformly distributed droplets and a high value of the liquid surface area — the most favourable condition for promoting the collection of impurities coming from the environment on the droplets surfaces. In other words, we recognize that a value of the capillary number of the order of magnitude of 10^{-4} is sufficiently high to sustain the motion of numerous small droplets able to collect gas impurities and, at the same time, sufficiently low to avoid excessive coalescence phenomena; a value that thereby promotes an effective self-cleaning mechanism of the heat exchanger surfaces.

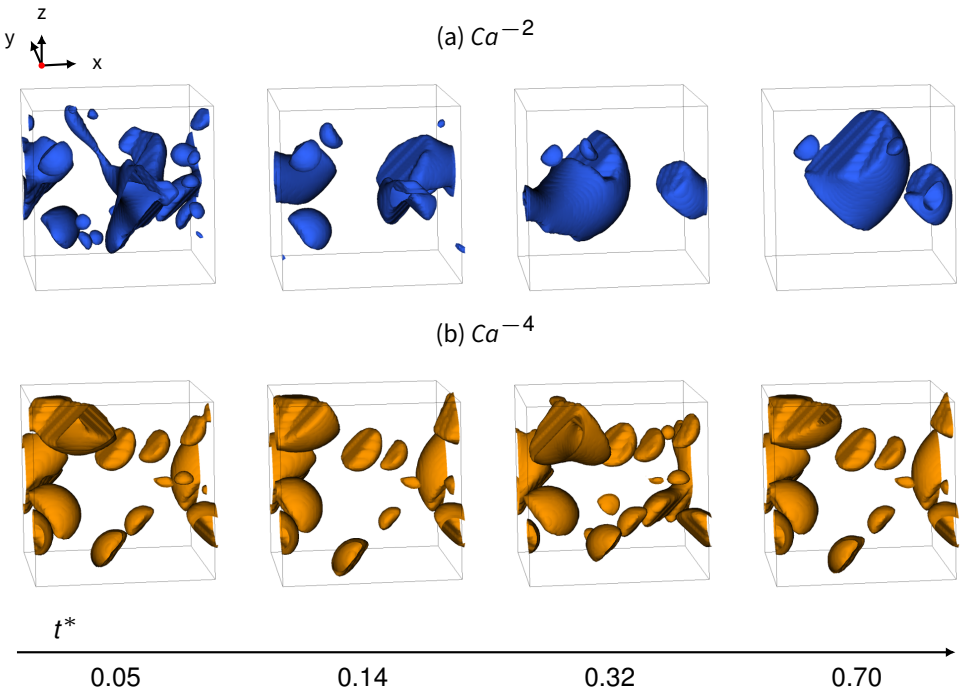

Figure 11: Zoom–in of a small region (size $10 \times 10 \times 10$ mm at $y = 8$ mm) from snapshots of simulations representing the two-phase flow patterns at four different times, for (a) $Ca \sim 10^{-2}$ (blue) and (b) $Ca \sim 10^{-4}$ (orange). The Jakob number is $Ja = 10^{-1}$. The pictures highlight the significant coalescence phenomena for $Ca \to Ca_{cr}$.

4. Final remarks

In the present study, we present a numerical investigation of fluid cooling, liquid condensation and two-phase flow pattern formation phenomena over corrugated heat exchanger surfaces. Different working operating conditions of the heat exchanger are simulated by means of the Lattice-Boltzmann methodology in order to identify the optimal one for promoting fouling-resistant and self-cleaning mechanisms of the surfaces. The heat exchanger heat duty and flow rate are quantified through the relevant non-dimensional Jakob and capillary numbers, which have been varied consistently to results obtained in our previous experimental analysis (Maggiolo et al., 2018), where an efficient self-cleaning mechanism has been observed.

By looking at time-dependent results of temperatures in absolute terms, the behaviour of the fluid is characterised by a rapid decrease from the ini-

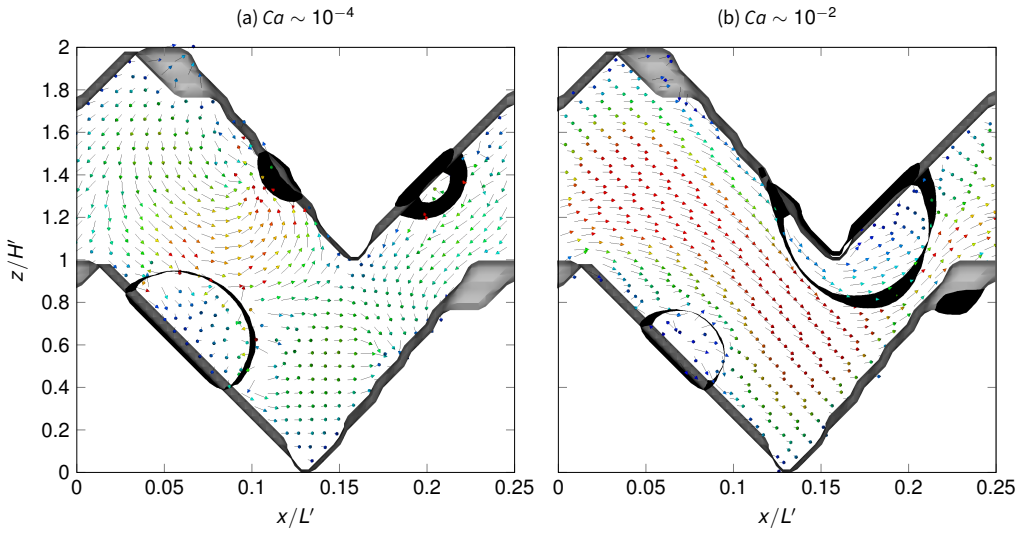

Figure 12: Snapshot of simulations representing the velocity (arrows) and density (black solid surfaces) fields. A small section of the size of $10 \times 0.17 \times 10$ mm at $y = 8$ mm and time $t^* = 0.70$ is depicted for $Ja = 10^{-1}$. The comparison between numerical solutions at $Ca \sim 10^{-4}$ (a) and $Ca \sim 10^{-2}$ (b) highlights the coalescence phenomena with a high capillary number induced by gas fluid forcing.

tial temperature value to the value of the cool plates, in all the considered cases. We note that, on the basis of the conventional design practice, in such thermodynamic conditions the heat exchanger is over-dimensioned. From another perspective, in order to enhance the self-cleaning effect, this over-dimensioning proves to be beneficial. By looking at the effective heat duty of the system, the fluid cooling process is found to be dependent on the Jakob number, with the slowest process occurring at the lowest Jakob number. In this case, the latent heat released during condensation is more significant than the sensible heat of the flow, so that the system is significantly warmed up by latent heat and the cooling process is slowed down. The slow cooling behaviour at low Jakob numbers is also characterised by a more uniformly distributed dropwise condensation. Rather than condensing in the valleys, as we observe for a finite Jakob number of $Ja \sim 1$, the droplets lay on the corrugated heat exchanger ribs where they can be easily transported away after having collected gas impurities. The mechanism of self-cleaning of the heat exchanger surfaces, which consists of the formation of small droplets which both collect and transport gas impurities, is therefore more easily triggered

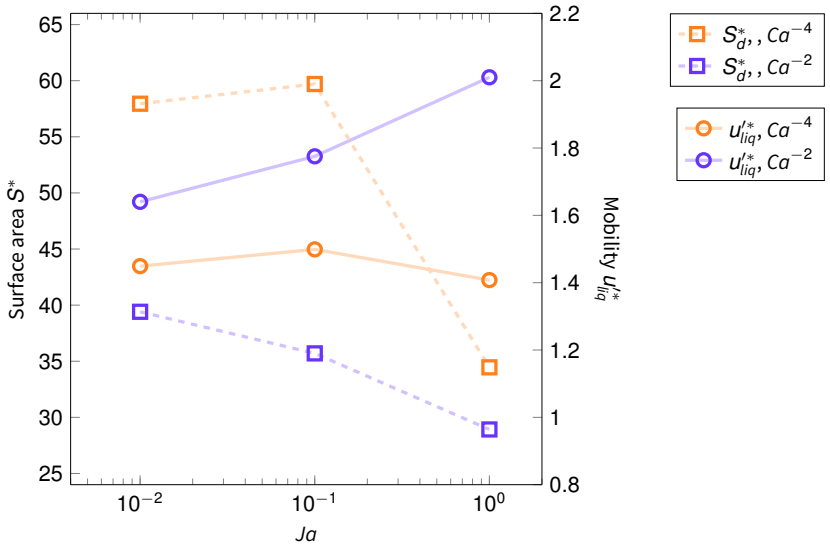

Figure 13: The self-cleaning efficiency of the heat exchanger quantified by the dimensionless mobility u'^{*}_{liq} (right axis), Eq. 16, and the dimensionless liquid-gas specific surface area $\mathcal{S}^{*}_{liq} = (\mathrm{d}\mathcal{S}(r)/\mathrm{d}r)\big|_{r\to 0}$ $(2H')$ (left axis), determined from Eq. 17. The figure highlights the influence of the structure parameters Ja and Ca – related to the operative conditions of the heat exchanger – on the two-phase flow patterns distribution at $t^{*} = 0.7$.

at low inlet temperatures of the heat exchanger. On the other hand, if the flow rate is too high, such small droplets tend to merge together. In fact, we observe a dramatic increase of coalescence phenomena at capillary numbers close to critical values which we noted can strongly limit the self-cleaning effect.

We therefore conclude that, in order to provoke and promote an efficient self cleaning process, low heat duties and flow rates are recommended, as opposed to the conventional heat exchanger design. For example, the herein unveiled optimal capillary and Jakob numbers, $Ca \sim 10^{-4}$ and $Ja \sim 0.1$, can be obtained by selecting the number of plates and, consequently, the designated mean gas velocity, and by controlling the inlet temperature and flow rate on the cooling side in order to adjust the sensible heat ΔT to be transferred over the passage through the heat exchanger. The present study thus lays the foundations for an effective design of self-cleaning heat exchangers, which are shown to be primarily governed by principles related to the two-phase flow rather than the heat transfer duty.

Conflicts of Interest

There are no conflicts to declare.

Acknowledgements

This work has been financed by the Swedish Energy Agency (project number 42206-1), the Centre for Combustion Science and Technology (CECOST) and the Swedish Centre for Biomass Gasification (SFC), and represents a part of a larger collaboration with the Division of Energy Technology at Chalmers University of Technology.

Alfa-Laval, 2018. Waste heat recovery. https://www.alfalaval.com/microsites/waste-heat-recovery/.

Banerjee, I., Pangule, R.C., Kane, R.S., 2011. Antifouling coatings: recent developments in the design of surfaces that prevent fouling by proteins, bacteria, and marine organisms. Advanced Materials 23, 690–718.

Biferale, L., Perlekar, P., Sbragaglia, M., Toschi, F., 2012. Convection in multiphase fluid flows using lattice boltzmann methods. Physical review letters 108, 104502.

Biferale, L., Perlekar, P., Sbragaglia, M., Toschi, F., 2013. Simulations of boiling systems using a lattice boltzmann method. Communications in Computational Physics 13, 696–705.

Blair, S.C., Berge, P.A., Berryman, J.G., 1996. Using two-point correlation functions to characterize microgeometry and estimate permeabilities of sandstones and porous glass. Journal of Geophysical Research: Solid Earth 101, 20359–20375.

Chambre, P., 1956. On the dynamics of phase growth. The Quarterly Journal of Mechanics and Applied Mathematics 9, 224–233.

Charach, C., Huleihil, M., Zarmi, Y., 1988. Perturbative analysis of planar phase change processes with time-dependent temperature at the boundary. Journal of applied physics 64, 4832–4837.

Chibbaro, S., 2008. Capillary filling with pseudo-potential binary lattice-boltzmann model. The European Physical Journal E 27, 99–106.

Cho, H.J., Preston, D.J., Zhu, Y., Wang, E.N., 2017. Nanoengineered materials for liquid–vapour phase-change heat transfer. Nature Reviews Materials 2, 16092.

De Maio, A., Palpacelli, S., Succi, S., 2011. A new boundary condition for three-dimensional lattice boltzmann simulations of capillary filling in rough micro-channels. Communications in Computational Physics 9, 1284–1292.

Guo, Z., Zheng, C., Shi, B., 2002. Discrete lattice effects on the forcing term in the lattice boltzmann method. Physical Review E 65, 046308.

Gupta, S.C., 2017. The Classical Stefan Problem: Basic Concepts, Modelling and Analysis with Quasi-Analytical Solutions and Methods. volume 45. Elsevier.

Kays, W.M., Crawford, M.E., Weigand, B., 2005. Convective heat and mass transfer.

Kilkovsky, B., Stehlik, P., Jegla, Z., Tovazhnyansky, L.L., Arsenyeva, O., Kapustenko, P.O., 2014. Heat exchangers for energy recovery in waste and biomass to energy technologies–i. energy recovery from flue gas. Applied Thermal Engineering 64, 213–223.

Larsson, A., Seemann, M., Neves, D., Thunman, H., 2013. Evaluation of performance of industrial-scale dual fluidized bed gasifiers using the chalmers 2–4-mwth gasifier. Energy & Fuels 27, 6665–6680.

Leach, R., Stevens, F., Langford, S., Dickinson, J., 2006. Dropwise condensation: experiments and simulations of nucleation and growth of water drops in a cooling system. Langmuir 22, 8864–8872.

Li, M.J., Tang, S.Z., Wang, F.l., Zhao, Q.X., Tao, W.Q., 2017. Gas-side fouling, erosion and corrosion of heat exchangers for middle/low temperature waste heat utilization: A review on simulation and experiment. Applied Thermal Engineering 126, 737–761.

Li, X., Pozrikidis, C., 1996. Shear flow over a liquid drop adhering to a solid surface. Journal of Fluid Mechanics 307, 167–190.

Maggiolo, D., Seemann, M., Thunman, H., Santos, O., Larsson, A., Sasic, S., Ström, H., 2018. Self-cleaning surfaces for heat recovery during industrial hydrocarbon-rich gas cooling: an experimental and numerical study. AIChE Journal .

Melo, L., Bott, T.R., Bernardo, C., 2012. Fouling science and technology. volume 145. Springer Science & Business Media.

Metwally, H., Manglik, R.M., 2004. Enhanced heat transfer due to curvature-induced lateral vortices in laminar flows in sinusoidal corrugated-plate channels. International Journal of Heat and Mass Transfer 47, 2283–2292.

Miljkovic, N., Wang, E.N., 2013. Condensation heat transfer on superhydrophobic surfaces. MRS bulletin 38, 397–406.

Müller-Steinhagen, H., Malayeri, M., Watkinson, A., 2005. Fouling of heat exchangers-new approaches to solve an old problem. Heat transfer engineering 26, 1–4.

Müller-Steinhagen, H., Malayeri, M., Watkinson, A., 2009. Heat exchanger fouling: environmental impacts. Taylor & Francis.

Odeh, A.S., 1959. Effect of viscosity ratio on relative permeability .

Rabou, L.P., Zwart, R.W., Vreugdenhil, B.J., Bos, L., 2009. Tar in biomass producer gas, the energy research centre of the netherlands (ecn) experience: an enduring challenge. Energy & Fuels 23, 6189–6198.

Rose, J., 1967. On the mechanism of dropwise condensation. International Journal of Heat and Mass Transfer 10, 755IN1757–756762.

Sbragaglia, M., Shan, X., 2011. Consistent pseudopotential interactions in lattice boltzmann models. Physical Review E 84, 036703.

Schleizer, A.D., Bonnecaze, R.T., 1999. Displacement of a two-dimensional immiscible droplet adhering to a wall in shear and pressure-driven flows. Journal of Fluid Mechanics 383, 29–54.

Shan, X., Chen, H., 1993. Lattice boltzmann model for simulating flows with multiple phases and components. Physical Review E 47, 1815.

Shi, X., Che, D., Agnew, B., Gao, J., 2011. An investigation of the performance of compact heat exchanger for latent heat recovery from exhaust flue gases. International Journal of Heat and Mass Transfer 54, 606–615.

Succi, S., 2001. The lattice Boltzmann equation: for fluid dynamics and beyond. Oxford university press.

Thunman, H., Seemann, M., Berdugo Vilches, T., Maric, J., Pallares, D., Ström, H., Berndes, G., Knutsson, P., Larsson, A., Breitholtz, C., et al., 2018. Advanced biofuel production via gasification–lessons learned from 200 man-years of research activity with chalmers' research gasifier and the gobigas demonstration plant. Energy Science & Engineering 6, 6–34.

Viovy, J.L., Beysens, D., Knobler, C.M., 1988. Scaling description for the growth of condensation patterns on surfaces. Physical Review A 37, 4965.

Vizika, O., Avraam, D., Payatakes, A., 1994. On the role of the viscosity ratio during low-capillary-number forced imbibition in porous media. Journal of colloid and interface science 165, 386–401.

Webb, R., 1981. Performance evaluation criteria for use of enhanced heat transfer surfaces in heat exchanger design. International Journal of Heat and Mass Transfer 24, 715–726.

Weisensee, P.B., Wang, Y., Hongliang, Q., Schultz, D., King, W.P., Miljkovic, N., 2017. Condensate droplet size distribution on lubricant-infused surfaces. International Journal of Heat and Mass Transfer 109, 187–199.

Yuan, P., Schaefer, L., 2006. A thermal lattice boltzmann two-phase flow model and its application to heat transfer problems—part 1. theoretical foundation. Journal of Fluids Engineering 128, 142–150.

Zhang, J., Tian, F., 2008. A bottom-up approach to non-ideal fluids in the lattice boltzmann method. EPL (Europhysics Letters) 81, 66005.